## VARIATIONAL PHASE FIELD FORMULATIONS OF POLARIZATION AND PHASE TRANSITION IN FERROELECTRIC THIN FILMS\*

QIANG DU<sup>†</sup>, RUOTAI LI<sup>‡</sup>, AND LEI ZHANG§

**Abstract.** The electric field plays an important role in ferroelectric phase transition. There have been numerous phase field formulations attempting to account for electrostatic interactions subject to different boundary conditions. In this paper, we develop new variational forms of the phase field electrostatic energy and the relaxation dynamics of the polarization vector that involves a hybrid representation in both real and Fourier variables. The new formulations avoid ambiguities appearing in earlier studies and lead to much more effective ways to perform variational studies and numerical simulations. Computations of phase transition and polarization switching in a single domain by applying the new formulations are provided as illustrative examples.

Key words. ferroelectric, electric field, phase transition, polarization switching, phase field, rare event

**AMS subject classifications.** 37N15, 49S05, 65K10, 65N22, 65Z05, 74N99, 78M30

**DOI.** 10.1137/19M1291431

1. Introduction. Ferroelectrics, first discovered in the 20th century, are materials possessing a spontaneous polarization that can be switched between energetically equivalent states in a single crystal by an electric field [7, 21]. The formation of domain structures when the temperature is cooled through the ferroelectric transition temperature (known as the Curie temperature) is a common feature of ferroelectric materials [20]. For example, from a cubic to tetragonal transformation in ferroelectrics, there are six possible domains separated by the so-called domain walls, with the polarization along or opposite to the [100], [010], and [001] directions of the cubic paraelectric phase [3]. The ferroelectric phase transition not only depends on domain wall motion but also is influenced by defects such as dislocations and preexisting domains as well as the electrostatic field [6, 26]. Thus, a fundamental understanding of the stability of domains and their responses to the external electric field and electrostatic interactions is critical for many applications of ferroelectrics. In particular, ferroelectric thin films have been extensively studied both theoretically and experimentally [2, 5, 12, 14, 22, 23, 25, 34] owing to their many potential applications in electronic and optical devices, including data storage, sensors, nonvolatile memories, thin film capacitors, etc. [7, 8, 15].

Recently, phase field method has been successfully applied to predict the temporal domain evolution during a ferroelectric transition, offering a powerful approach

<sup>\*</sup>Received by the editors October 4, 2019; accepted for publication (in revised form) April 23, 2020; published electronically June 29, 2020.

https://doi.org/10.1137/19M1291431

**Funding:** The work of the first author was partially supported by the NSF through grant DMS-1719699. The second author was supported by China Scholarship Council No. 201806010041. The work of the second and third authors was supported by the NSFC through grants 11861130351 and 11622102.

<sup>&</sup>lt;sup>†</sup>Department of Applied Physics and Applied Mathematics and Data Science Institute, Columbia University, New York, NY 10027 (qd2125@columbia.edu).

<sup>&</sup>lt;sup>‡</sup>Beijing International Center for Mathematical Research, Peking University, Beijing 100871, People's Republic of China (liruotai@pku.edu.cn).

<sup>§</sup>Beijing International Center for Mathematical Research, Center for Quantitative Biology, Peking University, Beijing 100871, People's Republic of China (zhangl@math.pku.edu.cn).

to characterize the detailed domain structures in three-dimensional (3D) ferroelectric thin films without any a priori assumptions with regard to the possible domain structures [19, 29]. The phase field method is able to predict not only the domain structures and the volume fractions of different orientation domains under the effect of applied external condition, such as the substrate constraint and electrostatic interactions, but also the detailed polarization switching during a ferroelectric transition [1, 6, 19, 26, 27, 29]. The phase field model of a ferroelectric thin film is briefly reviewed in section 2.

When using a phase field approach to model the ferroelectric thin film phase transition, the system usually involves both the polarization distributions, which are the main phase field variables to depict the polarization of ferroelectric materials, and the electrostatic potential that incorporates the electrostatic interactions. As a popular practice, their relation is described by the electrostatic equilibrium equation that can be derived from the Maxwell's equation. This implies that the electrostatic field is in its equilibrium state for a given polarization field and there is no free charge inside the film. Making use of this observation, the electrostatic potential could be acquired by solving the electrostatic equilibrium equation when given a polarization distribution during the ferroelectric phase transition. In this way the electrostatic energy and the electrostatic force could also be obtained [19].

We present new variational formulations for the phase field model involving electrostatic contributions under the no free charge assumption and with periodicity in directions parallel to the film. In section 3, the formulations are derived for the cases involving different boundary conditions (BCs) in the direction perpendicular to the film. By expressing the energy and forces in terms of the polarization distribution only and the electrostatic interactions implicitly accounted for, the new formulations avoid imposing additional constraints for energy minimization and temporal evolution and eliminate ambiguities that may surface in the previous formulations involving Lagrange multipliers. The analytically and explicitly formulated systems involve hybrid real space and Fourier space representations that are convenient to use in studies of energy landscape and relaxation dynamics. As an illustration, we present 3D numerical simulations of the phase transition and the polarization switching pathway in the cubic thin film of lead titanate (PbTiO<sub>3</sub>) based on the new formulations in section 4. Some conclusions are given in section 5.

2. Phase field model of a ferroelectric thin film. In the phase field approach, a ferroelectric domain structure in a thin film is often described by the primary order parameter  $P(x) = (P_1, P_2, P_3)$ , depicting the local spatial distribution of polarization in the 3D space, where x = (x, y, z) are the Cartesian coordinates. The temporal evolution of the polarization vector P is described by the time-dependent Ginzburg-Landau (TDGL) equations

(2.1) 
$$\frac{\partial P_i(\boldsymbol{x},t)}{\partial t} = -\eta \frac{\delta F}{\delta P_i(\boldsymbol{x},t)}, \quad i = 1, 2, 3,$$

where F is the total free energy of the system and  $\eta$  is the kinetic coefficient related to domain wall mobility.  $\delta F/\delta P_i(\boldsymbol{x},t)$  is the thermodynamic driving force for the spatial and temporal evolution of  $P_i(\boldsymbol{x},t)$ . The total free energy density includes three parts: the ferroelectric bulk free energy density  $f_{bulk}(\boldsymbol{P})$ , the domain wall energy density  $f_{wall}(\boldsymbol{P})$ , and the electrostatic energy density  $f_{ele}(\boldsymbol{P},\boldsymbol{E})$ . To present the free energy, we largely follow the phase field formulations given in [1, 6, 19, 20]. There were many other similar formulations used in studies on, e.g., domain wall interactions with line

charge defects [24], domain switching and the nucleation of domains under combined electromechanical BCs [34], and reduction to lower-dimensional models for thin films [12].

First, the bulk free and domain wall energy densities are described, respectively, using the expressions [20]

$$f_{bulk}(\mathbf{P}) = \alpha_1 (P_1^2 + P_2^2 + P_3^2) + \alpha_{11} (P_1^4 + P_2^4 + P_3^4)$$

$$+ \alpha_{12} (P_1^2 P_2^2 + P_2^2 P_3^2 + P_1^2 P_3^2) + \alpha_{111} (P_1^6 + P_2^6 + P_3^6)$$

$$+ \alpha_{112} [P_1^4 (P_1^2 + P_2^2) + P_2^4 (P_1^2 + P_3^2) + P_3^4 (P_1^2 + P_2^2)] + \alpha_{123} (P_1^2 P_2^2 P_3^2)$$

and

$$f_{wall}(P_{i,j}) = \frac{1}{2}G_{11}(P_{1,1}^2 + P_{2,2}^2 + P_{3,3}^2) + G_{12}(P_{1,1}P_{2,2} + P_{1,1}P_{3,3} + P_{2,2}P_{3,3})$$

$$(2.3) \qquad + \frac{1}{2}G_{44}[(P_{1,2} + P_{2,1})^2 + (P_{1,3} + P_{3,1})^2 + (P_{2,3} + P_{3,2})^2]$$

$$+ \frac{1}{2}G'_{44}[(P_{1,2} - P_{2,1})^2 + (P_{1,3} - P_{3,1})^2 + (P_{2,3} - P_{3,2})^2],$$

where  $\alpha_1$ ,  $\alpha_{11}$ ,  $\alpha_{12}$ ,  $\alpha_{111}$ ,  $\alpha_{112}$ ,  $\alpha_{123}$  are the Landau expansion coefficients and  $G_{11}$ ,  $G_{12}$ ,  $G_{44}$ ,  $G'_{44}$  are the domain wall energy coefficients, and here a comma in the subscript stands for spatial differentiation, e.g.,  $P_{i,j} = \partial P_i/\partial x_j$ , i, j = 1, 2, 3, with  $(x_1, x_2, x_3)$  denoting the Cartesian coordinates (x, y, z), respectively.

In this paper, we focus on the electrostatic energy and ignore possible surface and elastic energy contributions to the free energy. These simplifications are mainly for the purpose of illustration. In fact, we note that some detailed calculations of the elastic energy have been provided in the literature; see the case with periodic BCs [17] and the case where the substrate constraints are present [20].

The strategy proposed in this work is in a similar spirit to the microelasticity formulation developed in [17] that utilized an analytical formulation based on the Fourier representation under the spatial periodicity assumption. For the thin film, periodicities are assumed only along the film directions, while the other (nonperiodic) BCs are often necessary in the direction normal to film. Thus, we propose to adopt a hybrid Fourier and real space representation. Although the discussion in this work is limited to this special case, the extension and effective integration of hybrid formulations to more general cases involving additional energetic contributions can be expected and will be explored in subsequent works.

To begin our technical derivations, we recall Gauss's law for dielectrics:  $\nabla \cdot \mathbf{D} = \rho_f$ . Here  $\rho_f$  is the free charge density and  $\mathbf{D} = \epsilon \mathbf{E} + \mathbf{P}$  is the electric displacement, where  $\mathbf{E} = -\nabla \phi$  is the electric field with the electric potential  $\phi$  and  $\epsilon$  is the dielectric permittivity [13]. In the existing literature [1, 6, 26, 29], the electric energy in phase field models for dielectric systems has taken various mathematical forms that correspond to two different cases of the physical systems, namely,  $\rho_f = 0$  or  $\rho_f \neq 0$ . In the presence of free charges [1, 19], i.e.,  $\rho_f \neq 0$ , we suppose that the dielectric material brings in the free charge over time. If only the incremental free charges contribute the work to the electric energy, the energy density can be described by

(2.4) 
$$f_{ele} = -\frac{1}{2} \mathbf{E} \cdot \mathbf{D} = -\frac{1}{2} (\mathbf{E} \cdot \mathbf{P} + \epsilon |\mathbf{E}|^2).$$

In this case, Griffiths [13] argued that (2.4) is valid for linear dielectrics [13], i.e.,  $P = \epsilon_0 \xi E$ , where  $\epsilon_0$  is the vacuum permittivity and  $\xi$  is called the electric susceptibility

satisfying  $\epsilon = \epsilon_0(1+\xi)$ . Thus, (2.4) can be written as

(2.5) 
$$f_{ele} = -\frac{2\epsilon - \epsilon_0}{2(\epsilon - \epsilon_0)^2} \mathbf{P}^2,$$

which is directly expressed as a function of the polarization field  $\boldsymbol{P}$ . Hence, the electric energy and its variation can be readily obtained, similar to the bulk free energy and its variation. In fact, we have  $\frac{\delta F_{ele}(\boldsymbol{P})}{\delta \boldsymbol{P}} = -\frac{2\epsilon - \epsilon_0}{(\epsilon - \epsilon_0)^2} \boldsymbol{P}$ .

Let us make a note on this case of free charges. Usually, the coefficient  $\alpha_1$  of bulk free energy density in (2.2) has a linear temperature dependence based on the Curie–Weiss law; i.e.,  $\alpha_1 = \alpha(T - T_c)$ ,  $\alpha$  is a constant, and  $T_c$  is the Curie–Weiss temperature. By adding the electric energy from (2.5), the Curie–Weiss temperature actually becomes  $T'_c = T_c + \frac{2\epsilon - \epsilon_0}{2\alpha(\epsilon - \epsilon_0)^2}$ , meaning that the effect of the electric field can let the polarization occur more easily and the ferroelectric phase be more stable with respect to the temperature change.

On the other hand, if the electric field E or the electrostatic energy of a domain structure is considered to be self-electrostatic corresponding to the long-range electrostatic interaction of spontaneous polarizations [26, 29], it is natural to assume that the system satisfies the electrostatic equilibrium condition, i.e.,  $\rho_f = 0$ ; thus, the associated electric energy density in the case of bound charges is given by

$$(2.6) f_{ele} = -\frac{1}{2} \mathbf{E} \cdot \mathbf{P}.$$

Moreover, based on Gauss's law, the corresponding electrostatic equilibrium condition can be written as

(2.7) 
$$\epsilon \Delta \phi = \nabla \cdot \boldsymbol{P}.$$

Equation (2.7) holds in  $\Omega = (-L/2, L/2)^2 \times (0, h)$ , where L specifies the period along each of the directions parallel to the film and h specifies the film thickness.

In particular, if the electric potential  $\phi$  at the top and bottom surfaces of the film takes on constant values, we get

$$\phi|_{z=0} = c_1, \quad \phi|_{z=h} = c_2,$$

for two constants  $c_1$  and  $c_2$ . We call this set of condition the constant BC, particularly when  $c_1 = c_2$ , which is named the short-circuit BC.

We also consider the electric tip-induced BC [1] that is defined to model the applied electric field using piezoresponse force microscopy [6]. Then the potential distributions on the top and bottom surfaces are approximated by

(2.9) 
$$\phi|_{z=h} = \phi_{top}(x, y), \qquad \phi|_{z=0} = 0,$$

where

$$\phi_{top}(x,y) = \phi_0 \frac{\gamma^2}{(x-x_0)^2 + (y-y_0)^2 + \gamma^2}.$$

Here  $(x_0, y_0)$  is the location of the tip,  $\phi_0$  is a constant (peak of the potential), and  $\gamma$  stands for the effect length scale of the potential distribution.

If the normal component of the electric displacement  $\boldsymbol{D}$  is zero at that surface, then

(2.10) 
$$D_3|_{z=0} = D_3|_{z=h} = 0$$
 or, equivalently,  $(\epsilon \nabla \phi - \mathbf{P}) \cdot \vec{n}|_{z=0,h} = 0$ ,

where  $\vec{n}$  is the unit vector normal to the top and bottom surfaces. This set of conditions is named the open-circuit BC.

Viewing the equilibrium condition in (2.7) as an elliptic equation for the electric potential  $\phi$ , we see that conditions (2.8) and (2.9) are Dirichlet-type BCs, while (2.10) is a Neumann-type BC. Note that in the following calculations and derivations, the Dirichlet data  $c_1$  and  $c_2$  are not required to be constants unless specifically mentioned. With the above relation between  $\phi$  and polarization vector  $\mathbf{P}$ , we can calculate the electric potential and then obtain the electric field, the electrostatic energy, and its variation with respect to the polarization  $\mathbf{P}$ . The details are given in Appendices A and B.

Meanwhile, we note that if one wants to consider the energy density for the system in both the bound charge case and the free charge case in a unified setting, a straightforward way is to use a linear combination of (2.4) and (2.6), i.e.,

$$f_{ele} = -(\beta \mathbf{E} \cdot \mathbf{P} + (1 - \beta) \mathbf{E} \cdot \mathbf{D}),$$

for a constant  $\beta \in [0,1]$ . For the special case where  $\beta = 0$  or  $\beta = 1$ , we have the specified relation between E and P described above, respectively. However, for other values of  $\beta$ , it is unclear which specific relation between electric potential and polarization vector remains applicable.

3. New variational formulations of electrostatic interactions. We now focus on the case of bound charges with the electric energy density given by (2.6) and subject to the electrostatic equilibrium condition (2.7). We note that an explicit solution to (2.7) can be used to not only simplify the phase field energy formulation (2.6) but also derive an explicit mathematical expression of the functional variation of the electrostatic energy. This effectively allows us to find the explicit mathematical expression of the total driving force,

(3.1) 
$$\frac{\delta F}{\delta P_i} = \frac{\delta F_{bulk}}{\delta P_i} + \frac{\delta F_{wall}}{\delta P_i} + \frac{\delta F_{ele}}{\delta P_i}, \qquad i = 1, 2, 3,$$

in terms of the polarization vector  $\mathbf{P}$ . Here we use  $(x_1, x_2, x_3)$  to denote Cartesian coordinates (x, y, z), respectively. First, the bulk and the domain wall driving forces are given, respectively, by

(3.2) 
$$\frac{\delta F_{bulk}}{\delta P_i} = 2\alpha_1 P_i + 4\alpha_{11} P_i^3 + 2\alpha_{12} P_i \sum_{j \neq i} P_j^2 + 6\alpha_{111} P_i^5 + 4\alpha_{112} P_i^3 \sum_{j \neq i} P_j^2 + 4\alpha_{112} P_i \sum_{j \neq i} P_j^4 + 2\alpha_{123} P_i \prod_{j \neq i} P_j^2, \qquad i, j = 1, 2, 3,$$

and

(3.3) 
$$\frac{\delta F_{wall}}{\delta P_i} = -G_{11} \frac{\partial^2 P_i}{\partial x_i^2} - (G_{44} + G'_{44}) \sum_{j \neq i} \frac{\partial^2 P_i}{\partial x_j^2} + (G'_{44} - G_{12} - G_{44}) \sum_{j \neq i} \frac{\partial^2 P_j}{\partial x_i \partial x_j}, \qquad i, j = 1, 2, 3.$$

Natural Neumann-type BCs of the form

(3.4) 
$$\begin{cases} (G_{44} + G'_{44}) \frac{\partial P_1}{\partial x_3} + (G_{44} - G'_{44}) \frac{\partial P_3}{\partial x_1} = 0, \\ (G_{44} + G'_{44}) \frac{\partial P_2}{\partial x_3} + (G_{44} - G'_{44}) \frac{\partial P_3}{\partial x_2} = 0, \\ G_{11} \frac{\partial P_3}{\partial x_3} + G_{12} \left( \frac{\partial P_1}{\partial x_1} + \frac{\partial P_2}{\partial x_2} \right) = 0 \end{cases}$$

are also implied on the top  $(x_3 = z = 0)$  and bottom  $(x_3 = z = h)$  surfaces. The electrostatic driving forces, i.e., the variations of the energy given in (2.6), subject to the electrostatic equilibrium condition (2.7) and various BCs, are given by (3.5)

$$\frac{\delta F_{ele}}{\delta \boldsymbol{P}} = \left\{ \begin{array}{l} \nabla \phi - \frac{1}{2} \nabla \phi_2 \,, & \text{Dirichlet BC, e.g., constant BC (2.8), tip BC (2.9),} \\ \nabla \phi \,, & \text{Neumann BC, e.g., open-circuit BC (2.10),} \end{array} \right.$$

where  $\phi_2$  is an auxiliary potential. While more detailed derivations are given in Appendix B, we offer the main procedures on how the terms  $(\nabla \phi \text{ and } \nabla \phi_2)$  in (3.5) are determined. Let us use  $(\hat{\cdot})$  to denote the 2D Fourier series expansion due to the periodicity of  $\phi$  and P in the  $x_1$ - $x_2$  plane with  $(\lambda_1, \lambda_2)$  being the variables in the Fourier (frequency) space.

Let us work with  $\phi_2$  first for the constant and tip-induced boundary cases with more general discussions given in Appendix A. For the constant BC of (2.8), when  $c_1$  and  $c_2$  are all constants, we can take  $\nabla \phi_2 = \boldsymbol{a}$ , where  $\boldsymbol{a} = (0,0,a)^T$ ,  $a = \frac{c_2 - c_1}{h}$  with h being the film thickness.

As for the tip-induced BC of (2.9), based on the detailed calculation of  $\phi_2$  given in Appendix B.1.2, the function  $\phi_2$  is recovered from its Fourier representation given by

(3.6) 
$$\hat{\phi}_2(\lambda_1, \lambda_2, z) = \frac{\hat{\phi}_{top}(\lambda_1, \lambda_2)}{M(h)} (e^{|\lambda|z} - e^{-|\lambda|z}),$$

where  $\hat{\phi}_{top}$  is the Fourier expansion of the potential  $\phi|_{z=h} = \phi_{top}$  on the top surface,  $|\lambda| = \sqrt{\lambda_1^2 + \lambda_2^2}$ , and  $M(h) = e^{|\lambda|h} - e^{-|\lambda|h}$ .

Next, we condition the determination of  $\phi$  when  $(\lambda_1, \lambda_2) \neq (0, 0)$ , and (2.7) leads to

(3.7) 
$$\epsilon \left( \frac{\partial^2 \hat{\phi}}{\partial z^2} - \lambda_1^2 \hat{\phi} - \lambda_2^2 \hat{\phi} \right) = I \lambda_1 \hat{P}_1 + I \lambda_2 \hat{P}_2 + \frac{\partial \hat{P}_3}{\partial z} \triangleq f(\lambda_1, \lambda_2, z),$$

where  $I = \sqrt{-1}$  and  $f = f(\lambda_1, \lambda_2, z)$  denotes the 2D Fourier representation of the divergence on the right-hand side in (2.7). The function  $\phi$  is recovered from its Fourier representation given by

(3.8) 
$$\hat{\phi}(\lambda_1, \lambda_2, z) = C_1(\lambda_1, \lambda_2)e^{|\lambda|z} + C_2(\lambda_1, \lambda_2)e^{-|\lambda|z} + g(\lambda_1, \lambda_2, z),$$

where the function  $g = g(\lambda_1, \lambda_2, z)$  is defined by

(3.9) 
$$g(\lambda_1, \lambda_2, z) = \frac{1}{2|\lambda|\epsilon} \int_0^z [(e^{|\lambda|(z-s)} - e^{-|\lambda|(z-s)}) f(\lambda_1, \lambda_2, s)] ds.$$

As for the coefficients  $C = (C_1, C_2)^{\mathsf{T}}$  under the Dirichlet BC with  $c_2$  and  $c_1$  being the

top and bottom boundary data, respectively, we have

(3.10) 
$$C(\lambda_1, \lambda_2) = \frac{1}{M(h)} \begin{pmatrix} -\hat{c}_1(\lambda_1, \lambda_2)e^{-|\lambda|h} + \hat{c}_2(\lambda_1, \lambda_2) - g(\lambda_1, \lambda_2, h) \\ \hat{c}_1(\lambda_1, \lambda_2)e^{|\lambda|h} - \hat{c}_2(\lambda_1, \lambda_2) + g(\lambda_1, \lambda_2, h) \end{pmatrix},$$

where  $\hat{c}_1$  and  $\hat{c}_2$  are the Fourier representations of  $c_1$  and  $c_2$ , respectively.

For the constant BC (2.8) with  $c_1$  and  $c_2$  being constants, we have  $\hat{c}_1(\lambda_1, \lambda_2) = \hat{c}_2(\lambda_1, \lambda_2) = 0$ . So, (3.10) is effectively given by

$$C_2(\lambda_1, \lambda_2) = -C_1(\lambda_1, \lambda_2) = g(\lambda_1, \lambda_2, h)/M(h).$$

Meanwhile, under the tip-induced condition (2.9), we get instead

(3.11) 
$$C(\lambda_1, \lambda_2) = \frac{1}{M(h)} \begin{pmatrix} \hat{\phi}_{top}(\lambda_1, \lambda_2) - g(\lambda_1, \lambda_2, h) \\ -\hat{\phi}_{top}(\lambda_1, \lambda_2) + g(\lambda_1, \lambda_2, h) \end{pmatrix}.$$

Finally, under the open-circuit BC (2.10), we have

$$(3.12) \quad \boldsymbol{C}(\lambda_1, \lambda_2) = \frac{1}{|\lambda| M(h)} \begin{pmatrix} -\hat{P}_3(\lambda_1, \lambda_2, 0) e^{-|\lambda|h} + \hat{P}_3(\lambda_1, \lambda_2, h) - g_3(\lambda_1, \lambda_2, h) \\ -\hat{P}_3(\lambda_1, \lambda_2, 0) e^{|\lambda|h} + \hat{P}_3(\lambda_1, \lambda_2, h) - g_3(\lambda_1, \lambda_2, h) \end{pmatrix},$$

where

(3.13) 
$$g_3(\lambda_1, \lambda_2, h) = \frac{1}{2\epsilon} \int_0^h \left[ (e^{|\lambda|(h-s)} + e^{-|\lambda|(h-s)}) f(\lambda_1, \lambda_2, s) \right] ds$$

denotes the value of the partial derivative of  $g(\lambda_1, \lambda_2, z)$  with respect to the third variable z evaluated at z = h.

It is important to highlight that as  $f = f(\lambda_1, \lambda_2, z)$  is solely computed from the polarization field  $\mathbf{P}$ , so are the functions g,  $g_3$ , and  $\hat{\phi}$ . The numerical computations of the integrals associated with both g and  $g_3$  are highly dependent on the discretization of the functions and differential equations along the z direction. For illustration, here we adopt a finite difference approximation in the z direction on a uniform grid, which allows us to conveniently apply the composite Simpson rule based on the same grid points without further interpolations. We leave more detailed analysis of numerical discretization to subsequent works.

As a final note added for implementing the new variational formulations, we remark that for  $\lambda_1 = \lambda_2 = 0$ , (3.7) should be modified. For this special case, (3.7) can be simplified as a second-order ordinary differential equation for the real variable z with the solution given by

$$\hat{\phi}(0,0,z) = \int_0^z \hat{P}_3(0,0,s)ds + B_1 z + B_2,$$

where the  $B_1$  and  $B_2$  are determined by different BCs, e.g.,

$$\begin{cases} B_1 = \frac{1}{h} \left( \hat{c}_2 - \hat{c}_1 - \int_0^h \hat{P}_3(0, 0, s) ds \right), & B_2 = \hat{c}_1, & \text{for condition (2.8),} \\ B_1 = \frac{1}{h} \left( \hat{\phi}_{top}(0, 0) - \int_0^h \hat{P}_3(0, 0, s) ds \right), & B_2 = 0, & \text{for condition (2.9),} \\ B_1 = B_2 = 0, & \text{for condition (2.10).} \end{cases}$$

With the derivations above, (2.1) can be numerically solved by various methods. Although we leave detailed discussion on the numerical approximations to separate works, illustrative examples are presented later to show the effectiveness of the new formulations here.

- 4. Illustrative examples. We now present two numerical examples of the new variational formulations of the total energy and the driving forces by computing the equilibria and transition states. We adopt the steepest descent gradient dynamics (TDGL) for the former, which leads to the equilibria via temporal polarization evolution. For the latter, the transition state is the point (state) of the highest energy along the minimum energy path (MEP) between two local equilibria, which characterizes the morphology of the critical nucleus and the critical nucleation energy that determines the rate of a nucleation reaction [31, 30, 33]. In the last few decades, various numerical methods have been developed for saddle points and MEP calculation, e.g., the dimer method and its improvements [18, 28, 32], the nudged elastic band method [16], and the string method as well as its various improvements [9, 10, 11]. In this paper, we adopt a simplified string method in [11] to calculate the MEP to show the complete 180° polarization switching process described by the MEP connecting two equilibria.
- **4.1. Numerical results.** We take the lead titanate (PbTiO<sub>3</sub>) thin film as an example. The simulations are done on 3D computational domain of the size  $64\Delta x \times 64\Delta x \times 64\Delta x$  with the parameter  $\Delta x = 1.0$  nm referring to a uniform grid spacing in all three coordinate directions. The coefficients of the bulk free energy are exactly taken from [20]. Here the vacuum permittivity  $\epsilon_0 = 8.85 \times 10^{-12} Fm^{-1}$ , and the dielectric permittivity  $\epsilon = 100\epsilon_0$ . The isotropic domain wall energy coefficients are taken to be  $G_{11}/G_{110} = \frac{1}{2\Delta x}$ ,  $G_{12}/G_{110} = 0$ , and  $G_{44}/G_{110} = G'_{44}/G_{110} = \frac{1}{4\Delta x}$ , where  $G_{110}$  is related to the magnitude of grid spacing  $\Delta x$  via  $\Delta x = \sqrt{G_{110}/\alpha_0}$  and  $\alpha_0 = 1.7252 \times 10^8 C^{-1} m^2 N$ .

To simulate the temporal polarization change of the domain or the ferroelectric phase transition in the presence of an electric field, the relaxation system equation (2.1) is solved by using the semi-implicit Fourier spectral method with periodic BCs in the  $x_1$  and  $x_2$  axis along the film plane [4]. We compute several phase transitions by applying our newly derived electrostatic energy variation with different BCs in (3.5). In the figures presented here, different colors (red and blue) are used to represent the equivalent polarization magnitude and the corresponding polarization direction, i.e.,  $\mathbf{P} = (0,0,1)$  and  $\mathbf{P} = (0,0,-1)$ , respectively. The gradual change from the blue color to the red color represents the local dipole polarization magnitude and change in direction from -1 to 1 or vice versa.

Figure 1 shows the numerical simulation of the ferroelectric phase transition started from a random domain distribution to an equilibrium in the presence of an electric field. In the example, the electric field in the form of (2.6) is used with the constant BC (2.8). After nondimensionalization, the constant BC is used so that the electric potential is 0 on the top surface ( $\phi|_{z=h}=0$ ) and 10 on the bottom surface ( $\phi|_{z=0}=10$ ). From the result, the random domains gradually disappear under a large enough electric potential during the evolution, and the final polarization domain is formed to minimize the electric effect.

Figure 2 shows the ferroelectric phase transition started from a tip-induced-like domain configuration to an equilibrium in the presence of an electric field. Figure 2A shows the sliced view (at y=0) of the initial polarization state of Figure 2B in the X-Z plane, and the scale and direction of black arrows illustrate the local dipole magnitude and direction of each unit cell in the X-Z plane. In this case, the electric field is in the form of (2.6) with the tip-induced BC (2.9). The tip-induced electric potential is zero on the bottom surface of the film and satisfies the distribution  $\phi_{top}(x,y) = -\frac{2}{x^2+y^2+1}$  on the top surface, i.e.,  $\phi_0 = -2$ ,  $\gamma = 1$ , and  $(x_0, y_0) = (0, 0)$ . While the electric field

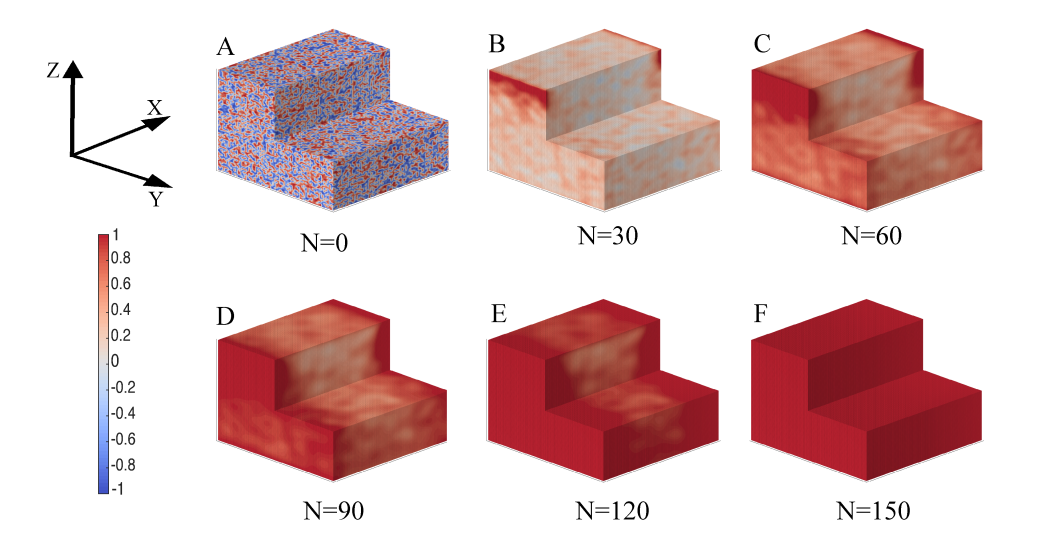


Fig. 1. Ferroelectric phase transition from an initial random polarization distribution to an equilibrium under the constant BC. A–F: The simulated domain changes in the 3D configuration space at different iteration steps, e.g., N=0, 30, and 150, respectively.

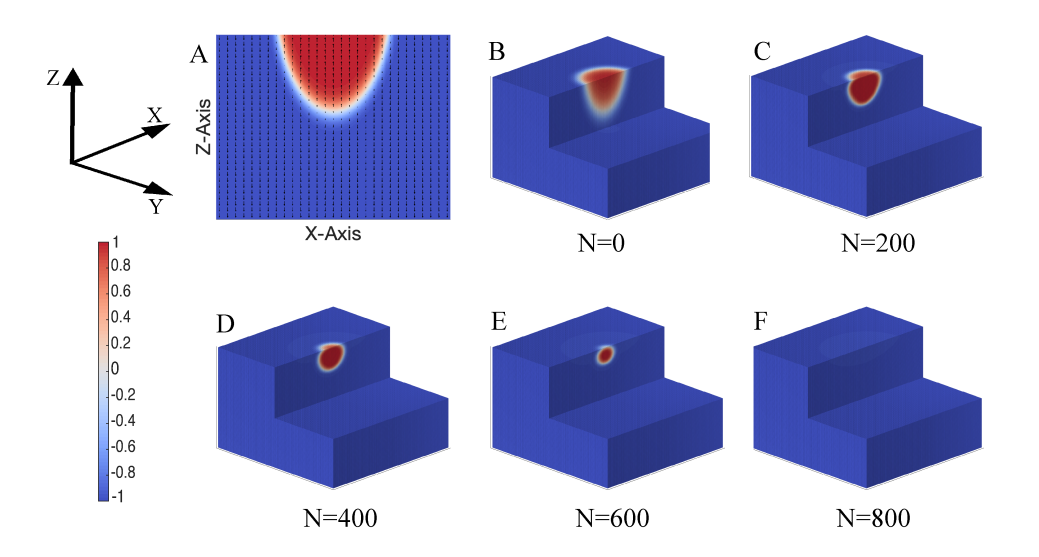


FIG. 2. Ferroelectric phase transition from an initial polarization distribution to an equilibrium under the tip-induced BC. A: The sliced view (at y=0) of the initial polarization state of the ferroelectric domain in the X-Z plane (blue and red-shade plane in the schematic). B–F: The simulated domain changes in the 3D configuration space at different iteration steps, e.g., N=0,200, and 800, respectively.

effect may generate a local polarization switching, numerical simulation shows that it cannot induce a complete polarization switching if the initial domain (nucleus) is not large enough or the electric field is not strong enough.

Next, we apply the simplified string method to compute the complete process of 180° polarization switching from  $\mathbf{P} = (0,0,-1)$  to  $\mathbf{P} = (0,0,1)$  with the new variational form. In Figure 3, we plot the MEP of the total polarization switching

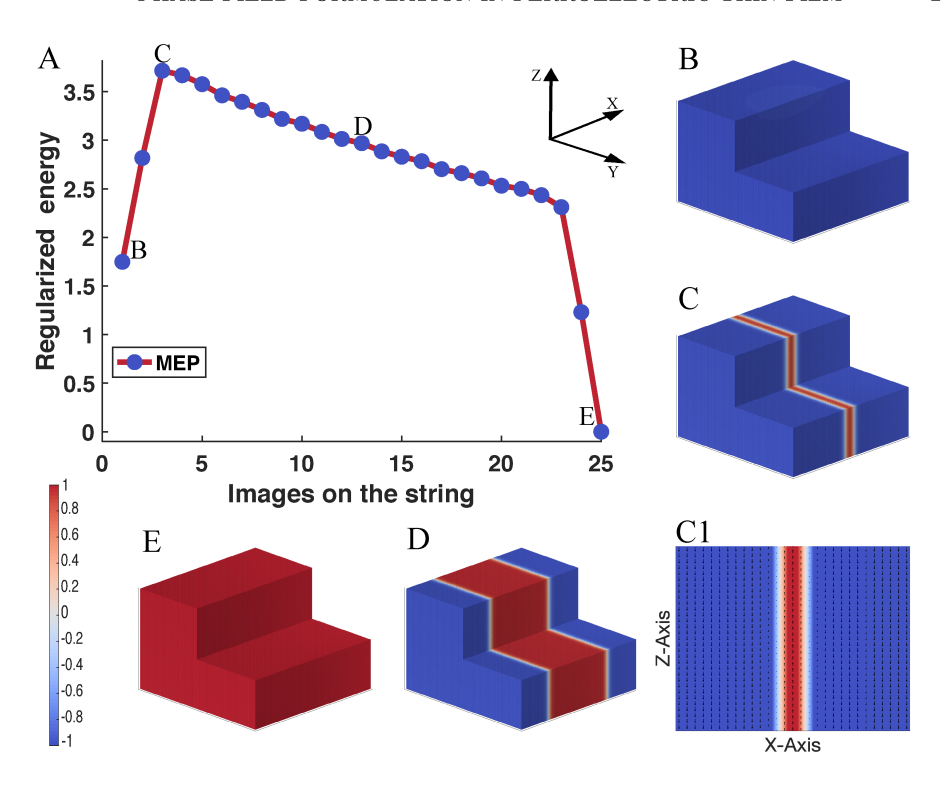


FIG. 3. Computed MEP shows the ribbon-like 180° polarization switching process under the constant BC. A: The MEP of polarization switching connecting the initial polarization state (B) with the final polarization state (E) by passing through the critical nucleus (C). B: The initial steady polarization state ( $\mathbf{P} = (0,0,-1)$ ). C: A ribbon-like critical nucleus corresponding to the point with the highest energy on the MEP. C1: Sliced view of the critical nucleus (at y=0) showing the domain pattern in the X-Z plane. D: An intermediate state after passing the critical nucleus, corresponding to the point D on the MEP. E: The final steady polarization state ( $\mathbf{P} = (0,0,1)$ ).

process, which corresponds to a ribbon-like pattern geometrically. In the presence of an electric field, Figure 3C shows the configuration of the critical nucleus as a thin polarization switching domain with a sharp interface, which gives the width of interface  $\delta \approx \sqrt{G_{11}/\alpha_0}$  and  $\delta = \sqrt{\Delta x/2}$  in this case. We slice the configuration of the nucleus along y=0 axis to show its domain pattern in the 2D X-Z plane clearly, with the scale and direction of black arrows indicating the local dipole magnitude and direction of each unit cell in the X-Z plane. Moreover, the width of the thin domain gets enlarged with the increase of energy, and once the critical nucleus is formed to overcome the energy barrier, the switched polarization domain continues to grow until the final equilibrium state  $\mathbf{P}=(0,0,1)$  is achieved.

5. Conclusions/summary. With the newly formulated phase field energy involving electrostatic energy contributions, the variation of the electrostatic energy and the total free energy becomes straightforward. It eliminates the requirement to impose constraints in the variational calculation and avoids the use of associated Lagrange multipliers. The explicitly formulated expression of the driving force makes it convenient for numerical simulations and avoids ambiguity. It also helps to improve simulation accuracy, as the electrostatic equilibrium equation is now given by an exact explicit analytical solution.

By using the new electrostatic energy variation under different BCs with suitable electrostatic potential, we are able to accurately perform the complete phase transition process of the 180° polarization switching and find the critical nucleus with a thin polarization domain in 3D configuration space while demonstrating the effectiveness of the mathematical formulation. The shapes of critical nuclei could be varied under different electric fields and driving forces. More detailed discussions on other types of polarization switching process will be illustrated in a later work.

Although the current work only focuses on the ferroelectric phase transition involving electrostatic contributions, the other contributions, such as the elastic energy, can be also taken into account. We expect that a similar approach can be applied to more general phase field models for ferroelectric and ferromagnetic materials, which will be pursued in the future.

Appendix A. Calculating the electric field under different BCs. We have already presented the precise functional forms of the electrostatic energy given, respectively, in (2.4) and (2.6). We now present in more detail calculating the solution of the electrostatic equilibrium equation (2.7) subject to either (2.8) or (2.10) and the functional variation of the energy form (2.6) under different BCs.

We first discuss how to calculate the electric field and the electric potential  $\phi$  from the polarization field. Applying the 2D Fourier expansion on (2.7), as the  $\phi$  and  $\mathbf{P}$  are periodic in the X-Y (or equivalently the  $x_1$ - $x_2$ ) plane, (2.7) becomes (3.7), i.e.,

$$\hat{\phi}(\lambda_1, \lambda_2, z) = \frac{1}{L^2} \int_{-\frac{L}{2}}^{\frac{L}{2}} \int_{-\frac{L}{2}}^{\frac{L}{2}} \phi(x, y, z) e^{-I(\frac{2\pi\lambda_1 x + 2\pi\lambda_2 y}{L})} dx dy.$$

For each  $\lambda_1$  and  $\lambda_2$ , (3.7) can be taken as an independent scalar linear ordinary differential equation of  $\hat{\phi}$  in real variable z, and we can easily find its general solution in the form of (3.8).

By performing a 2D Fourier expansion on the electric BC, (2.8), (2.10), and (2.9), the unknown coefficients  $C_1 = C_1(\lambda_1, \lambda_2)$  and  $C_2 = C_2(\lambda_1, \lambda_2)$  can be determined, respectively. More specifically, let g(z) and  $g_3(z)$  be shorthand notations of the functions  $g(\lambda_1, \lambda_2, z)$  and  $g_3(\lambda_1, \lambda_2, z)$  given by (3.9) and (3.13), respectively, with  $f(\lambda_1, \lambda_2, z)$  being defined by (3.7). We then have the following  $2 \times 2$  linear systems.

For the Dirichlet BC (including the special constant BC by (2.8)),

(A.1) 
$$\begin{cases} C_1 + C_2 = \hat{c}_1(\lambda_1, \lambda_2), \\ C_1 e^{|\lambda|h} + C_2 e^{-|\lambda|h} + g(h) = \hat{c}_2(\lambda_1, \lambda_2). \end{cases}$$

For the tip-induced BC by (2.9), we have a special case of the above, namely,

(A.2) 
$$\begin{cases} C_1 + C_2 = 0, \\ C_1 e^{|\lambda|h} + C_2 e^{-|\lambda|h} + g(h) = \hat{\phi}_{top}(\lambda_1, \lambda_2). \end{cases}$$

For the open-circuit (Neumann) BC by (2.10), we have

(A.3) 
$$\begin{cases} C_1|\lambda| - C_2|\lambda| = \hat{P}_3(\lambda_1, \lambda_2, 0), \\ 2|\lambda|(C_1 e^{|\lambda|h} - C_2 e^{-|\lambda|h}) + g_3(h) = \hat{P}_3(\lambda_1, \lambda_2, h), \end{cases}$$

where  $g_3(h)$  is the value of  $g_3(z)$  at z equal to h. By solving these linear equations, we can get the coefficients  $C_1$  and  $C_2$  corresponding to different BCs, as given in

(3.10), (3.11), and (3.12), respectively. The electric potential and electric field can be easily obtained from the Fourier expansion (or the discrete inverse Fourier transform on lattice points) of (3.8) and its derivatives, e.g.,

(A.4) 
$$\phi(x,y,z) = L^2 \sum_{\lambda_1,\lambda_2 = -\infty}^{\infty} \hat{\phi}(\lambda_1,\lambda_2,z) e^{I\frac{2\pi\lambda_1 x}{L}} e^{I\frac{2\pi\lambda_2 y}{L}}$$

and

$$(A.5) \qquad \left(\begin{array}{c} \frac{\partial \phi}{\partial x} \\ \frac{\partial \phi}{\partial y} \end{array}\right) = L^2 \sum_{\lambda_1, \lambda_2 = -\infty}^{\infty} I\left(\begin{array}{c} \lambda_1 \\ \lambda_2 \end{array}\right) \hat{\phi}(\lambda_1, \lambda_2, z) e^{I\frac{2\pi\lambda_1 x}{L}} e^{I\frac{2\pi\lambda_2 y}{L}},$$

while

(A.6) 
$$\frac{\partial \phi}{\partial z} = L^2 \sum_{\lambda_1, \lambda_2 = -\infty}^{\infty} [|\lambda| (C_1 e^{|\lambda|z} - C_2 e^{-|\lambda|z}) + g_3(z)] e^{I\frac{2\pi\lambda_1 x}{L}} e^{I\frac{2\pi\lambda_2 y}{L}}.$$

Consequently, the electrostatic energy can also be obtained.

For the Poisson equation (2.7) with a more general Dirichlet BC in the z direction, we can make use of the linearity of the operator  $\Delta$  and decompose the solution  $\phi$  of (2.7) into  $\phi = \phi_1 + \phi_2$  with  $\phi_1$ ,  $\phi_2$  satisfying

(A.7) 
$$\begin{cases} \epsilon \Delta \phi_1 = \nabla \cdot \mathbf{P} \\ \phi_1|_{z=0} = \phi_1|_{z=h} = 0 \end{cases} \text{ and } \begin{cases} \epsilon \Delta \phi_2 = 0 \\ \phi_2|_{z=0} = c_1, \quad \phi_2|_{z=h} = c_2. \end{cases}$$

The total solution for (2.7) under this type of BC is  $\phi = \phi_1 + \phi_2$ , and the total electric field is  $\nabla \phi = \nabla \phi_1 + \nabla \phi_2$ . This works in general without requiring the Dirichlet data  $c_1$  and  $c_2$  being constants.

Now we adopt the same idea and notations to calculate  $\phi_2$  and its derivatives under the Dirichlet BC. For the special case by (2.8), when both  $c_1$  and  $c_2$  are constants, the solution  $\phi_2$  with these boundary constants has the form of  $\phi_2 = az + b$   $(a = \frac{c_2 - c_1}{h})$  and  $b = c_1$ . Thus, the special case leads to  $\phi = \phi_1 + az + b$ ,  $\nabla \phi_2 = a$ , and  $\nabla \phi = \nabla \phi_1 + a$ , where  $a = (0,0,a)^{\mathrm{T}}$ .

In general, we may apply the 2D Fourier expansion in the X-Y plane to solve the Laplace equation for  $\phi_2$ , i.e.,

(A.8) 
$$\frac{d^2 \hat{\phi}_2}{dz^2} - (\lambda_1^2 + \lambda_2^2) \hat{\phi}_2 = 0.$$

The solution of the homogeneous second-order ordinary differential equation with respect to real variable z by (A.8) has the form

(A.9) 
$$\hat{\phi}_2(\lambda_1, \lambda_2, z) = C_1(\lambda_1, \lambda_2)e^{|\lambda|z} + C_2(\lambda_1, \lambda_2)e^{-|\lambda|z},$$

where  $|\lambda|$  is the same as used above. Performing a 2D Fourier expansion on the BC (2.8), the unknown coefficients  $C_1$  and  $C_2$  can be determined by solving the linear equations

(A.10) 
$$\begin{cases} C_1(\lambda_1, \lambda_2) + C_2(\lambda_1, \lambda_2) = \hat{c}_1, \\ C_1(\lambda_1, \lambda_2) e^{|\lambda| h} + C_2(\lambda_1, \lambda_2) e^{-|\lambda| h} = \hat{c}_2. \end{cases}$$

Thus, the solution of  $C_1$  and  $C_2$  could be given by

(A.11) 
$$C_1(\lambda_1, \lambda_2) = \frac{\hat{c}_2 - \hat{c}_1 e^{-|\lambda|h}}{e^{|\lambda|h} - e^{-|\lambda|h}}, \qquad C_2(\lambda_1, \lambda_2) = \frac{\hat{c}_1 e^{|\lambda|h} - \hat{c}_2}{e^{|\lambda|h} - e^{-|\lambda|h}}$$

Appendix B. Calculation of the electrostatic energy variation of (2.6) under different BCs.

**B.1.** Energy and energy variation under the Dirichlet BC. To calculate the electrostatic energy in the form of (2.6) and its energy variation under the Dirichlet BC, we adopt the splitting idea above, and the electrostatic energy in the form (2.6) can be rewritten as

$$F_{ele} = \int_{\Omega} f_{ele} \ dV = \int_{\Omega} \frac{1}{2} (\nabla \phi_1 \cdot \mathbf{P} + \nabla \phi_2 \cdot \mathbf{P}) \ dV.$$

Thus, we only need to handle the term  $\nabla \phi_1$ , as the  $\phi_2$  is independent of  $\boldsymbol{P}$  according to (A.7). For notational convenience, we just use  $\phi_1(\boldsymbol{P})$  to denote the dependence of  $\phi_1$  on P, which is a linear operator and can be easily found by the left part of (A.7). More specifically,  $\phi_1(\boldsymbol{P})$  refers to the solution of the Poisson equation subject to the homogeneous Dirichlet boundary for a given  $\boldsymbol{P}$ , i.e.,  $\Delta \phi_1(\boldsymbol{P}) = \frac{1}{\epsilon} div(\boldsymbol{P})$  in the domain and  $\phi_1 = 0$  on the top and bottom boundary surfaces (periodicity in the film plane). Meanwhile,  $\nabla \phi_1(\boldsymbol{P})$  refers to the electric field corresponding to the auxiliary potential  $\phi_1$ , and we calculate the  $Fr\acute{e}chet$  derivative of electrostatic energy at  $\boldsymbol{P}$  along the direction  $\vec{Q}$  as

(B.1) 
$$\frac{\partial F_{ele}(\boldsymbol{P}+l\vec{Q})}{\partial l}|_{l=0} = \frac{1}{2} \int_{\Omega} [\nabla \phi_1(\boldsymbol{P}) \cdot \vec{Q} + \nabla \phi_1(\vec{Q}) \cdot \boldsymbol{P} + \nabla \phi_2 \cdot \vec{Q}] \ dV,$$

where l is a scalar. Using the divergence theorem, Green's identity, and the periodicity of P,  $\vec{Q}$  and  $\phi_1(P)$ ,  $\phi_1(\vec{Q})$  in the X-Y plane and the zero Dirichlet condition for the latter pair on the top and bottom surfaces, we get

$$\int_{\Omega} \nabla \phi_{1}(\vec{Q}) \cdot \mathbf{P} dV = -\int_{\Omega} \phi_{1}(\vec{Q}) \operatorname{div} \mathbf{P} dV 
= -\epsilon \int_{\Omega} \phi_{1}(\vec{Q}) \Delta \phi_{1}(P) dV 
= -\epsilon \int_{\Omega} \Delta \phi_{1}(\vec{Q}) \phi_{1}(P) dV 
= -\int_{\Omega} \operatorname{div} \vec{Q} \phi_{1}(P) dV 
= \int_{\Omega} \vec{Q} \cdot \nabla \phi_{1}(P) dV.$$

Combining the above derivation and results in (B.1), we can get the variation of electrostatic energy in the form (2.6), under the Dirichlet BC (2.8), as

(B.3) 
$$\frac{\delta F_{ele}}{\delta \mathbf{P}} = \nabla \phi_1 + \frac{1}{2} \nabla \phi_2 = \nabla \phi - \frac{1}{2} \nabla \phi_2.$$

**B.1.1.** The case with constant BC. A particular case of the Dirichlet BC is the constant BC by (2.8), with  $c_1$  and  $c_2$  being constants in the X-Y plane. For (2.6), we end up with the following form for the electrostatic energy:

$$F_{ele} = \int_{\Omega} \frac{1}{2} (\nabla \phi_1 \cdot \boldsymbol{P} + \boldsymbol{a} \cdot \boldsymbol{P}) \ dV.$$

The energy variation is

$$\frac{\delta F_{ele}}{\delta \mathbf{P}} = \nabla \phi - \frac{1}{2} \nabla \phi_2 = \nabla \phi - \frac{1}{2} \mathbf{a} .$$

**B.1.2.** The case with tip-induced BC. The tip-induced BC by (2.9) is another special case of the Dirichlet BC. Following the results presented in Appendix A above and with  $\phi = \phi_1 + \phi_2$ , we easily get that the electrostatic energy variation with respect to polarization vector P in the energy density form, (2.6), is

$$\frac{\delta F_{ele}}{\delta \boldsymbol{P}} = \nabla \phi_1 + \frac{1}{2} \nabla \phi_2 = \nabla \phi - \frac{1}{2} \nabla \phi_2 \,.$$

The potential  $\phi_2$  satisfies

(B.4) 
$$\begin{cases} \Delta \phi_2 = 0 \\ \phi_2|_{z=0} = 0, \quad \phi_2|_{z=h} = \phi_0 \left[ \frac{\gamma^2}{(x-x_0)^2 + (y-y_0)^2 + \gamma^2} \right]. \end{cases}$$

The solution can be determined as discussed previously in Appendix A. In this special case, (A.11) leads to

$$C_1(\lambda_1, \lambda_2) = -C_2(\lambda_1, \lambda_2) = \frac{\hat{\phi}_{top}(\lambda_1, \lambda_2)}{e^{|\lambda|h} - e^{-|\lambda|h}}.$$

Similarly, we can get the solution of  $\phi_2$  in both real and Fourier variables under the Dirichlet BC through the 2D Fourier expansion, i.e., (A.4), and in this way the gradient of  $\phi_2$  can also be computed, e.g., through (A.5), and

(B.5) 
$$\frac{\partial \phi_2}{\partial z} = L^2 \sum_{\lambda_1 = -\infty}^{\infty} \sum_{\lambda_2 = -\infty}^{\infty} |\lambda| (C_1 e^{|\lambda|z} - C_2 e^{-|\lambda|z}) e^{I \frac{2\pi\lambda_1 x}{L}} e^{I \frac{2\pi\lambda_2 y}{L}}.$$

Thus, the total electrostatic potential can be obtained by summing up the solution of the two parts in (A.7).

**B.2.** Electrostatic energy and its variation in an open circuit. We note that the electrostatic energy in (2.6) is

$$F_{ele} = \int_{\Omega} f_{ele} \ dV = \int_{\Omega} \frac{1}{2} \nabla \phi \cdot \boldsymbol{P} \ dV.$$

We adopt the same idea used before to calculate the  $Fr\acute{e}chet$  derivative of the electrostatic energy in this case. For the  $Fr\acute{e}chet$  derivative of electrostatic energy at P along the direction  $\vec{Q}$ , we can use the same expression as given in (B.1). But in this case,  $\phi_1$  is replaced by  $\phi$ , and  $\phi(\vec{Q})$  means the solution of the Poisson equation subject to the Neumann BC for a given  $\vec{Q}$ , i.e.,  $\Delta\phi(\vec{Q}) = \frac{1}{\epsilon} {\rm div}(\vec{Q})$  in the domain, and  $\epsilon\nabla\phi(\vec{Q})\cdot\vec{n}=\vec{Q}\cdot\vec{n}$  on the top and bottom boundary surfaces (periodicity in the film plane), where  $\vec{n}$  is the unit vector normal to the boundary surface.

For the integral of  $\nabla \phi(\vec{Q}) \cdot P$ , we note that (2.7) still holds. By using the divergence theorem, Green's identity, and the periodicity of P,  $\phi(P)$ ,  $\vec{Q}$  and  $\phi(\vec{Q})$  in the X-Y plane as well as the Neumann BC for the two pairs on the top and bottom

surface boundaries, respectively, we get

$$\int_{\Omega} \nabla \phi(\vec{Q}) \cdot \mathbf{P} \, dV$$

$$= \int_{\partial \Omega} \phi(\vec{Q}) \mathbf{P} \cdot dS - \int_{\Omega} \phi(\vec{Q}) \operatorname{div} \mathbf{P} dV$$

$$= \int_{\partial \Omega} \phi(\vec{Q}) \mathbf{P} \cdot dS + \epsilon \left( \int_{\Omega} \nabla \phi(\vec{Q}) \cdot \nabla \phi(\mathbf{P}) dV - \int_{\partial \Omega} \phi(\vec{Q}) \nabla \phi(\mathbf{P}) \cdot dS \right)$$

$$= \int_{\partial \Omega} [\phi(\vec{Q}) (\mathbf{P} - \epsilon \nabla \phi(\mathbf{P}))] \cdot dS + \epsilon \left( \int_{\partial \Omega} \phi(\mathbf{P}) \nabla \phi(\vec{Q}) \cdot dS - \int_{\Omega} \phi(\mathbf{P}) \Delta \phi(\vec{Q}) \, dV \right)$$

$$= \epsilon \int_{\partial \Omega} \phi(\mathbf{P}) \nabla \phi(\vec{Q}) \cdot dS - \int_{\Omega} \phi(\mathbf{P}) \operatorname{div} \vec{Q} \, dV$$

$$= \int_{\partial \Omega} [\phi(\mathbf{P}) (\epsilon \nabla \phi(\vec{Q}) - \vec{Q})] \cdot dS + \int_{\Omega} \nabla \phi(\mathbf{P}) \cdot \vec{Q} \, dV$$

$$= \int_{\Omega} \nabla \phi(\mathbf{P}) \cdot \vec{Q} \, dV,$$

where dS denotes the normal surface area element, and from the derivation above, combining the  $Fr\acute{e}chet$  derivative in (B.1), we can easily get that the variation of the energy form (2.6), under the open-circuit BC, is

(B.7) 
$$\frac{\delta F_{ele}}{\delta \mathbf{P}} = \nabla \phi(\mathbf{P}).$$

It should be noted that under the Neumann BC, the solutions of the Poisson equation differ from each other by a constant. This is unimportant in general, as the goal is to obtain the electric field  $\nabla \phi$  that is unique according to the Poisson equation in this case when given a polarization vector  $\boldsymbol{P}$ .

**Acknowledgments.** We would like to thank Prof. Long-Qing Chen, Dr. Yu-Lan Li, and Dr. Bo Wang for fruitful discussions.

## REFERENCES

- J. Britson, P. Gao, X. Pan, and L. Chen, Phase field simulation of charged interface formation during ferroelectric switching, Acta Mater., 112 (2016), pp. 285–294, https://doi.org/10.1016/j.actamat.2016.04.026.
- [2] P. CHANDRA AND P. LITTLEWOOD, A Landau primer for ferroelectrics, in The Physics of Ferroelectrics: A Modern Perspective, K. Rabe, C. Ahn, and J.-M. Triscone, eds., Topics Appl. Phys. 105, Springer, New York, 2007, pp. 69–116, http://link.springer.com/content/ pdf/10.1007/978-3-540-34591-6\_3.
- [3] L. Chen, Phase-field method of phase transitions/domain structures in ferroelectric thin films: A review, J. Amer. Ceram. Soc., 91 (2008), pp. 1835–1844, https://doi.org/10.1111/j. 1551-2916.2008.02413.x.
- [4] L. CHEN AND J. SHEN, Application of semi-implicit Fourier-spectral method to phase field equations, Comput. Phys. Commun., 108 (1998), pp. 147–158, https://doi.org/10.1016/ S0010-4655(97)00115-X.
- [5] K. Choi, M. Biegalski, Y. Li, A. Sharan, J. Schubert, R. Uecker, P. Reiche, Y. Chen, X. Pan, V. Gopalan, L. Chen, D. Schlom, and C. Eom, Enhancement of ferroelectricity in strained batio 3thin films, Science, 306 (2004), p. 1005, https://doi.org/10.1126/science. 1103218.
- [6] S. CHOUDHURY, J. ZHANG, Y. LI, L. CHEN, Q. JIA, AND S. KALININ, Effect of ferroelastic twin walls on local polarization switching: Phase-field modeling, Appl. Phys. Lett., 93 (2008), 162901, https://doi.org/10.1063/1.2993330.

- [7] L. CROSS, Ferroelectric ceramics: Tailoring properties for specific applications, in Ferroelectric Ceramics, N. Setter and E. Colla, eds., Birkhäuser Verlag, Basel, 1993, pp. 1–85. http://cds.cern.ch/record/113309.
- [8] D. Damjanovic, Ferroelectric, dielectric and piezoelectric properties of ferroelectric thin films and ceramics, Rep. Progr. Phys., 61 (1998), 1267, https://iopscience.iop.org/article/10. 1088/0034-4885/61/9/002.
- [9] Q. Du and L. Zhang, A constrained string method and its numerical analysis, Commun. Math. Sci., 7 (2009), pp. 1039–1051, https://projecteuclid.org/euclid.cms/1264434143.
- [10] W. E, W. Ren, and E. Vanden-Eijnden, String method for the study of rare events, Phys. Rev. B, 66 (2002), https://doi.org/10.1103/PhysRevB.66.052301.
- [11] W. E, W. Ren, and E. Vanden-Eijnden, Simplified and improved string method for computing the minimum energy paths in barrier-crossing events, J. Chem. Phys., 126 (2007), 164103, https://doi.org/10.1063/1.2720838.
- [12] A. GAUDIELLO AND K. HAMDACHE, The polarization in a ferroelectric thin film: Local and nonlocal limit problems, ESAIM Control Optim. Calc. Var., 19 (2013), pp. 657–667, https://doi.org/10.1051/cocv/2012026.
- [13] D. GRIFFITHS, Introduction to Electrodynamics, Prentice Hall, Englewood Cliffs, NJ, 3rd ed., 1999, pp. 160–202.
- [14] J. Haeni, P. Irvin, W. Chang, R. Uecker, P. Reiche, Y. Li, S. Choudhury, W. Tian, M. Hawley, B. Craigo, A. Tagantsev, X. Pan, S. Streiffer, L. Chen, S. Kirchoefer, J. Levy, and D. Schlom, Room-temperature ferroelectricity in strained srtio3, Nature, 430 (2004), pp. 758–761, https://doi.org/10.1038/nature02773.
- [15] G. HAERTLING, Ferroelectric ceramics: History and technology, J. Amer. Ceram. Soc., 82 (1999), 797, https://doi.org/10.1111/j.1151-2916.1999.tb01840.x.
- [16] G. Henkelman and H. Jónsson, A climbing image nudged elastic band method for finding saddle points and minimum energy paths, J. Chem. Phys., 113 (2000), https://doi.org/10. 1063/1.1329672.
- [17] A. KHACHATURYAN, Theory of Structural Transformations in Solids, Wiley, New York, 1983, https://www.osti.gov/biblio/5821133.
- [18] A. LEVITT AND C. ORTNER, Convergence and cycling in Walker-type saddle search algorithms, SIAM J. Numer. Anal., 55 (2017), pp. 2204–2227, https://doi.org/10.1137/16M1087199.
- [19] Y. LI, L. CHEN, G. ASAYAMA, D. SCHLOM, M. ZURBUCHEN, AND S. STREIFFER, Ferroelectric domain structures in srbi2nb209 epitaxial thin films: Electron microscopy and phase-field simulations, J. Appl. Phys., 95 (2004), pp. 6332-6340, https://doi.org/10.1063/1.1707211.
- [20] Y. Li, S. Hu, Z. Liu, And L. Chen, Effect of substrate constraint on the stability and evolution of ferroelectric domain structures in thin films, Acta Mater., 50 (2002), https://doi.org/ 10.1016/S1359-6454(01)00360-3.
- [21] M. LINES AND A. GLASS, Principles and Applications of Ferroelectrics and Related Materials, Oxford University Press, Oxford, 1977, http://cds.cern.ch/record/367846.
- [22] N. PERTSEV AND V. KOUKHAR, Polarization instability in polydomain ferroelectric epitaxial thin films and the formation of heterophase structures, Phys. Rev. Lett., 84 (2000), p. 3722, https://doi.org/10.1103/PhysRevLett.84.3722.
- [23] J. SPECK, A. SEIFERT, W. POMPE, AND R. RAMESH, Domain configurations due to multiple misfit relaxation mechanisms in epitaxial ferroelectric thin films. II. Experimental verification and implications, J. Appl. Phys., 76 (1994), p. 477, https://doi.org/10.1063/1.357098.
- [24] Y. Su and C. Landis, Continuum thermodynamics of ferroelectric domain evolution: Theory, finite element implementation, and application to domain wall pinning, J. Mech. Phys. Solids, 55 (2007), pp. 280–305, https://doi.org/10.1016/j.jmps.2006.07.006.
- [25] D. Tenne, X. XI, Y. LI, L. Chen, A. Soukiassian, M. Zhu, A. James, J. Lettieri, D. Schlom, W. Tian, and X. Pan, Absence of low-temperature phase transitions in epitaxial batio3 thin films, Phys. Rev. B, 69 (2004), 174101, https://doi.org/10.1103/PhysRevB. 69.174101.
- [26] J. WANG AND T. ZHANG, Phase field simulations of polarization switching-induced toughening in ferroelectric ceramics, Acta Mater., 55 (2007), pp. 2465-2477, https://doi.org/10.1016/ i.actamat.2006.11.041.
- [27] J. ZHANG AND Q. Du, Numerical studies of discrete approximations to the Allen-Cahn equation in the sharp interface limit, SIAM J. Sci. Comput., 31 (2009), pp. 3042–3063, https://doi. org/10.1137/080738398.
- [28] J. ZHANG AND Q. Du, Shrinking dimer dynamics and its applications to saddle point search, SIAM J. Numer. Anal., 50 (2012), pp. 1899–1921, https://doi.org/10.1137/110843149.
- [29] J. ZHANG, Y. LI, S. CHOUDHURY, L. CHEN, Y. CHU, F. ZAVALICHE, M. CRUZ, R. RAMESH, AND Q. JIA, Computer simulation of ferroelectric domain structures in epitaxial bifeo3 thin films, J. Appl. Phys., 103 (2008), 094111, https://doi.org/10.1063/1.2927385.

- [30] L. ZHANG, L. CHEN, AND Q. DU, Diffuse-interface approach to predicting morphologies of critical nucleus and equilibrium structure for cubic to tetragonal transformations, J. Comput. Phys., 229 (2010), pp. 6574–6584, https://doi.org/10.1016/j.jcp.2010.05.013.
- [31] L. ZHANG, L. Q. CHEN, AND Q. Du, Morphology of critical nuclei in solid-state phase transformations, Phys. Rev. Lett., 98 (2007), https://doi.org/10.1103/PhysRevLett.98.265703.
- [32] L. Zhang, Q. Du, and Z. Zheng, Optimization-based shrinking dimer method for finding transition states, SIAM J. Sci. Comput., 38 (2016), pp. 528-544, https://doi.org/10.1137/ 140972676.
- [33] L. ZHANG, W. REN, A. SAMANTA, AND Q. Du, Recent developments in computational modelling of nucleation in phase transformations, npj Comput. Mater., 2 (2016), https://doi.org/10. 1038/npjcompumats.2016.3.
- [34] W. Zhang and K. Bhattacharya, A computational model of ferroelectric domains. Part I: Model formulation and domain switching, Acta Mater., 53 (2005), pp. 185–198, https://doi.org/10.1016/j.actamat.2004.09.016.